Forecasting the Ocean's Optical Environment Using the BioCast System

BY JASON KEITH JOLLIFF,
SHERWIN LADNER,
RICHARD CROUT,
PAUL LYON,
KENNETH MATULEWSKI,
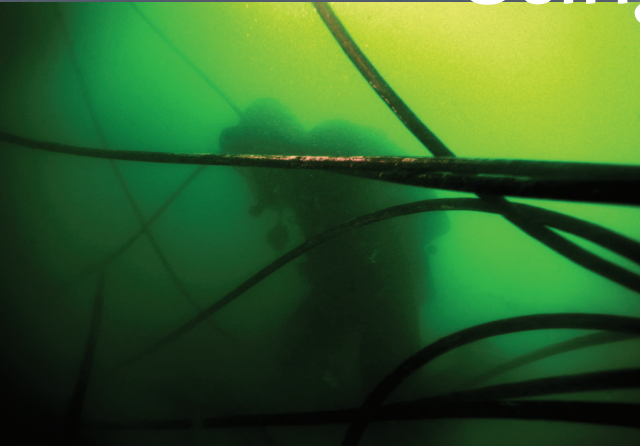ROBERT A. ARNONE,
AND DAVID LEWIS

Figure 1. From blue to brown, clear to murky, the US Navy must operate in the full range of the ocean's optical conditions. (background) The Littoral Combat Ship USS *Freedom* (LCS 1) in the Pacific Ocean. (top left) A US Navy diver assigned to Mobile Diving Salvage Unit (MDSU) 2 at work during operations off the coast of Bahrain. (middle left) US Navy Special Warfare Combatant Crewmen (SWCC) assigned to Special Boat Team-22 training in the Pearl River estuary system on the Louisiana/Mississippi border, USA. (bottom left) US Navy diver during underwater mine countermeasures training in the Middle East. *Photo credits: US Navy*

ABSTRACT. The Bio-Optical Forecasting (BioCast) system is a model that provides the US Navy with short-term forecasts of the ocean's optical environment. The forecasts are required to support a broad spectrum of naval operations, including mine countermeasures and anti-submarine and expeditionary warfare missions. The BioCast system works by treating any geo-referenced surface ocean optical property provided via the US Navy's satellite data processing systems as a prognostic state variable. BioCast will then ingest operational ocean model velocity forecasts and calculate the three-dimensional optical property (pseudo-tracer) transport. BioCast verification statistics generated via forecast comparison to "next-day" satellite images show superior performance over 24-hour persistence of composite satellite data. Future operational modifications to BioCast, such as complex internal transformation submodels, must demonstrate superior performance to the established benchmark metrics and/or persistence over the operational forecast time horizon. Future BioCast applications will expand to include an interface with three-dimensional system performance simulation techniques that will predict how specific US Navy sensors will perform in the ocean's optical environment.

INTRODUCTION

The role of ocean optics in naval warfare dates back to ancient times. In the first century BCE, the Roman general Gaius Julius Caesar watched from the shores of Quiberon Bay as the outmatched Roman fleet nonetheless delivered a decisive victory over the Veneti Gaul ships-of-war (Caesar, 56 BCE). The fifth century writer Vegetius informs us that the Roman scouting vessels of Caesar's Gallic campaign were painted a "Venetian" blue, thereby blending into the rich turquoise-tinted waters of what is now France's Morbihan coast (Vegetius, 432, est.). The enhanced Roman advantages of surprise and stealth upon seafaring vessels of superior craftsmanship may have ultimately facilitated the close-range deployment of the Roman grappling hooks used to smash down enemy sailing rigs. The conflict was then reduced to a land battle upon floating barges, and on land the Romans were indomitable. Subsequent Roman

maritime forays farther north and across the English Channel from mainland Gaul, in contrast, were hardly surprising to the vigilant tribes of the British Isles (Caesar, 55 BCE). One may speculate that perhaps blue-painted boats manned with blue-uniformed sailors and marines would have been rather conspicuous against the turbid gray waves marking the entryway to the riotous North Sea.

Two thousand years later, observing and forecasting the ocean's optical properties remains critical to the practice of naval warfare. For example, mines and underwater Improvised Explosive Devices (IEDs) are a potentially devastating asymmetric threat to naval operations and overseas commerce. Detection of underwater mines with airborne, towed, or autonomous underwater platforms can be severely impeded by sustained water column turbidity. Similarly, naval diver deployment for mine countermeasure and expeditionary warfare missions is also impacted by

reduced underwater visibility. And as in Caesar's day, variability of water-leaving radiance (i.e., the apparent color of the ocean to the above-water observer) must be considered when naval tactics require stealth and surprise.

Hence, the propagation of radiance through the ocean, the ocean's optical environment, is pertinent to a broad spectrum of naval operations (Figure 1). Information dominance of the battlespace environment requires knowledge of the ocean's present optical state and some estimate of its future optical state across the mission planning time horizon. The US Naval Research Laboratory (NRL) has sought to meet this requirement by forging a bridge between increasingly capable technological advancements in two areas: (1) satellite ocean color remote sensing, and (2) numerical ocean circulation models and their associated computational environment.

Satellite ocean color remote sensing has evolved substantially since the 1978 launch of the pioneering Coastal Zone Color Scanner (CZCS). Subsequent satellite-based sensors, such as the Sea-Viewing Wide-Field-of-View Sensor (SeaWiFS) and the Moderate Resolution Imaging Spectroradiometer (MODIS), have amply demonstrated the broad scientific applications of synoptic detection of water-leaving radiance. Concomitant advances in atmospheric correction and product algorithms have been incorporated into NRL's Automated Optical Processing System (AOPS; Ladner et al., 2013). AOPS is geared toward naval applications and is used to render operational products from

multiple satellite sensors for areas of strategic concern (Figure 2). AOPS provides satellite-imaging capability to the US Naval Oceanographic Office for direct support of the US Navy's operations.

Operational satellite-based multispectral ocean color imaging continues with new sensors and platforms, such as the Visible Infrared Imager Radiometer Suite (VIIRS) sensor on board the Suomi National Polar-orbiting Partnership satellite. However, a new generation of sensors is also being tested and developed to render hyperspectral, high spatial resolution images of the ocean surface (Chang et al., 2004). NRL's Hyperspectral Imager of the Coastal Ocean (HICO) sensor (Corson and Davis, 2011; Lewis et al., 2013), mounted on the International Space Station in 2009, provides 100 m horizontal resolution hyperspectral images from around the world (Figure 3). These HICO data resolve increasingly intricate details of coastal optical dynamics that would have been nearly impossible to obtain 40 years ago.

Simultaneous to satellite ocean color progress, ocean circulation models have become increasingly capable—pushing toward finer scales of spatiotemporal resolution and resolving more complex ocean phenomena. For example, the operational global ocean forecasting systems of 12 years ago were performing at 1/8° (~ 14 km) horizontal resolution (Rhodes et al., 2002). The new systems under development will provide ~ 3.5 km horizontal resolution forecasts of ocean density and velocity fields (see Metzger et al., 2014, in this issue). This new generation of global forecasting models will also provide boundary conditions for coastal nested modeling systems that seek to resolve physical ocean processes down to the subkilometer horizontal scale (see Rowley et al., 2014, and Allard et al., 2014, both in this issue). The potential merger of these modeling and remote-sensing advances suggests an optical sensing and forecasting capability that is accurate down to the scale of the individual operator (e.g., a naval diver). The remaining question is: how to proceed?
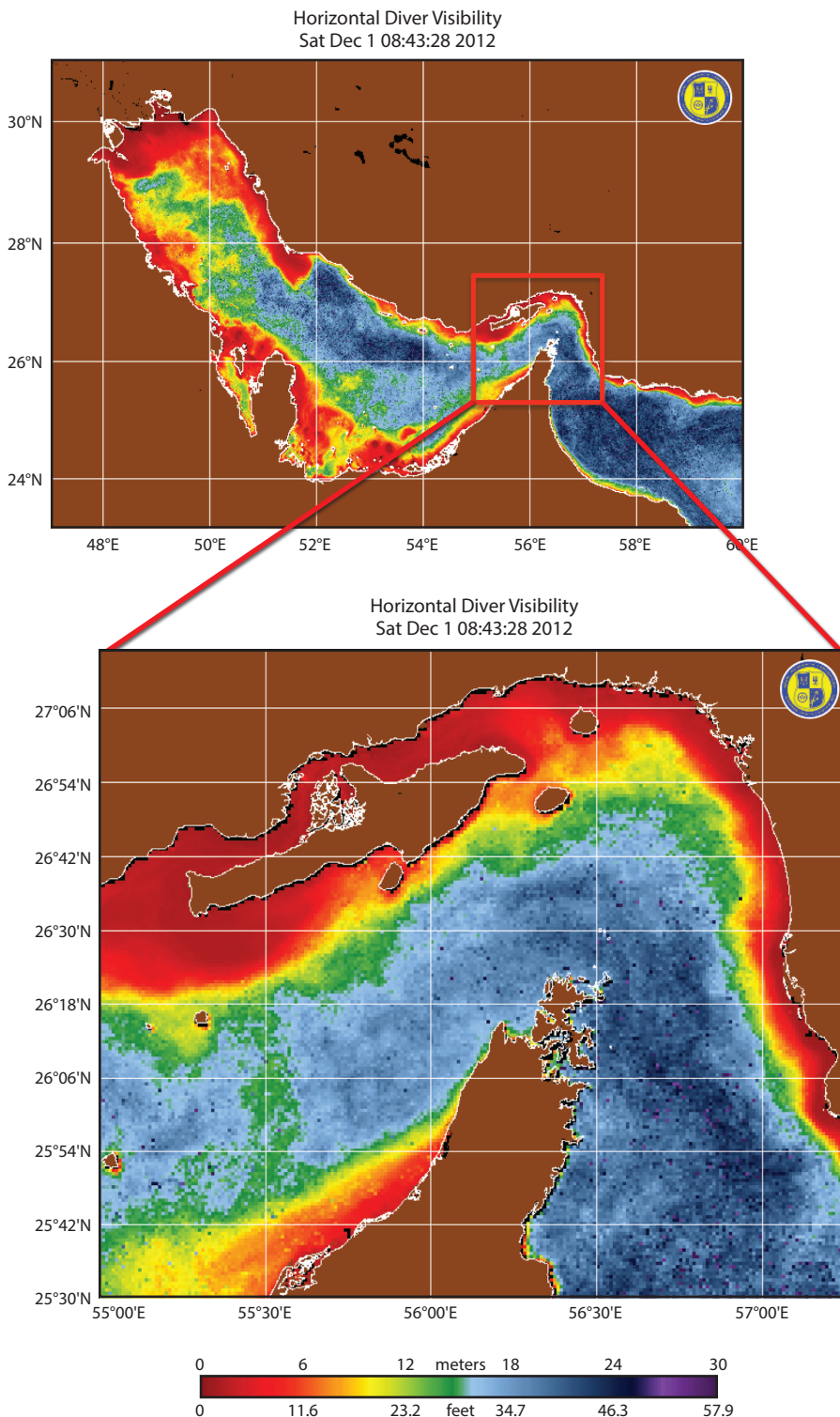

Figure 2. Automated Optical Processing System (AOPS) Horizontal Diver Visibility, 1,000 m resolution, Arabian Gulf (top) and zoomed in to the red box around the Straits of Hormuz (bottom).

BIOCAST: THEORETICAL FOUNDATION

On the strength of one link in the cable
Dependeth the might of the chain;
Who knows when thou mayest be tested?
So live that thou bearest the strain!

– Admiral Ronald A. Hopwood in
"The Laws of the Navy," *Reef Points*, 1920

Synoptic, satellite-based images of ocean surface optical features (Figure 3) are the manifestation of a long chain of causal events that cannot be grasped by a single scientific discipline. An appropriate investigative starting place is the point of detection: radiance impacting the satellite sensor. Having accounted for the intervening atmosphere, light propagation out of the ocean is fundamentally a boundary value problem: the inherent optical properties (IOPs) of seawater and its dissolved and particulate constituents confront some initial source of radiance. Given these IOPs and some radiant quantity as boundary values, the physical process of light propagation is addressed via the radiative transfer equation (Mobley, 1994). A mechanistic understanding of the time-dependent changes in the distribution of the seawater constituents that are manifest as IOP variability, however, requires an understanding of the nexus between ocean circulation and many varied biogeochemical processes of the upper ocean.

In coastal areas, optically active and highly variable seawater constituents may include organic matter derived from the breakdown of vascular plant and other organic materials in soils and sediments. Inorganic grains of clays, silts, and sands may also be suspended in the water column and contribute heavily to the scattering of light. Ubiquitous in these environments are the optical properties of microalgal cells, their associated photosynthetic and photoprotective pigments, and the nonliving organic matter derived from the mortality, herbivore ingestion, and decay of these phytoplankton.

These diverse materials are formally linked to IOPs via the additive properties of optical coefficients. For example, the total beam attenuation coefficient (c_t, or beam-c) at a given wavelength (λ) is the sum of the total absorption (a_t) and scattering (b_t) coefficients:

$$c_t(\lambda) = a_t(\lambda) + b_t(\lambda) \qquad (1)$$

Beam attenuation is important because it serves as a basis for many underwater visibility and sensor performance estimates. As an example, horizontal diver visibility may be estimated as inversely proportional to beam attenuation (Zaneveld and Pegau, 2003). The

Jason Keith Jolliff (*jolliff@nrlssc.navy.mil*) *is Oceanographer,* **Sherwin Ladner** *is Oceanographer, and* **Richard Crout** *is Supervisory Oceanographer, all at the Naval Research Laboratory (NRL), Stennis Space Center, MS, USA.* **Paul Lyon** *is Oceanographer and* **Kenneth Matulewski** *is Senior Oceanographer, both at the Naval Oceanographic Office, Stennis Space Center, MS, USA.* **Robert A. Arnone** *is Research Professor, University of Southern Mississippi, Stennis Space Center, MS, USA.* **David Lewis** *is Oceanographer, NRL, Stennis Space Center, MS, USA.*
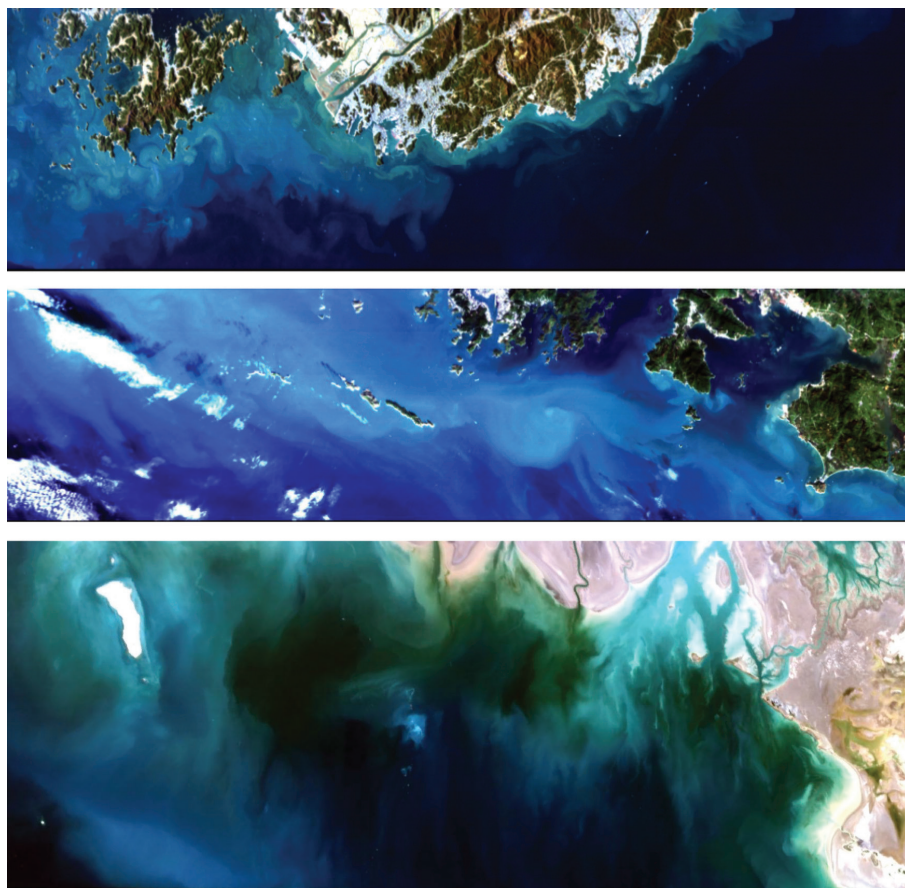

Figure 3. Hyperspectral Imager of the Coastal Ocean (HICO) true color images of (top to bottom): Pusan, South Korea; Hong Kong, China; and Tigris and Euphrates River outflow, northern Arabian Gulf.

physical meaning of Equation 1 is also easy to comprehend: a photon traveling through water along a specific direction (path) will encounter optically active matter and will either be absorbed (a_t) or scattered (b_t) to some other direction.

Total absorption and scattering coefficients are typically broken down into a summation of different contributing constituents. A complete and exhaustive accounting of all optically active materials for a given ocean region is impractical. Hence, optically active materials are often grouped into general classes of optical contributors:

$$a_t(\lambda) = a_{SW}(\lambda) + a_{NL}(\lambda) + a_{SS}(\lambda) \qquad (2)$$

and

$$b_t(\lambda) = b_{SW}(\lambda) + b_{\phi}(\lambda) + \\ b_{NL}(\lambda) + b_{SS}(\lambda) \qquad (3)$$

where the subscripts refer to the constituent class: SW is pure seawater, ϕ is the living phytoplankton contribution, NL is nonliving organic matter, and SS is suspended inorganic sediments. A breakdown of the percentage contribution to a given total IOP from each constituent class at a specified wavelength may then be used as a basis for optical water mass classification (Schofield et al., 2004). Wavelengths for some material classes in our example may be dropped as negligible toward absorption or scattering and alternate constituent class partitions are certainly possible.

Optically active constituent classes are thus associated with a fluctuating material quantity. This mass concentration of materials (M_x: mass of material per unit volume of seawater) is then governed by a mass conservation equation of the general form

$$\frac{\delta M_x}{\delta t} = [\nabla \cdot (\mathbf{v}M_x)] + F + Q \qquad (4)$$

that may be broken down into separable processes: a simplified term for physical transport $[\nabla \cdot (\mathbf{v}M_x)]$, boundary value fluxes (F), and internal transformations (Q). If Equation 4 is applied to a delineated coastal region of the ocean, the boundaries will include potential mass fluxes (F) at the lateral land/sea boundaries and the potential addition/removal of mass at the seaward spatial boundaries of the region considered. Internal transformations (Q) may vary widely depending on the material class of the constituent. For example, sediments may be subject to settling and coagulation; living phytoplankton population growth and decline is subject to the functioning and structure of the marine ecosystem.

Optical-mass transforms that define the relationships between specific mass (the amount of material in a fixed volume of seawater) and some characteristic inherent optical property at a reference wavelength (e.g., the absorption coefficient at 440 nm) are required to express the optical consequences of mass conservation. An additional spectral function is also required to translate the optical property at a single reference wavelength to IOPs across a spectral region (e.g., the visible spectrum, ~ 390–700 nm). As an example, chromophoric dissolved organic matter (CDOM) is a chemically complex fraction of the total dissolved organic matter pool that contributes substantially to the absorption of visible light in marine waters (Siegel et al., 2002). CDOM optical properties are highly variable in relation to organic matter concentration (μmol Carbon L^{-1}) and may change substantially due to multifaceted interactions with the environment, such as exposure to ultraviolet radiation (Vodacek et al., 1997; Kowalczuk et al., 2010).

Similar mass-specific optical

complexities arise for suspended sediment types and grain size (e.g., Binding et al., 2005) and the complexities of phytoplankton populations (e.g., Cunningham et al., 2003). The latter point is often simplified as bulk "chlorophyll-a" primary pigment measurements. Nevertheless, oceanographers should be ever cognizant of the vast optical complexity attendant to microalgal biodiversity. There are over 4,000 species of marine phytoplankton (Sournia et al., 1991). The bulk optical properties of the phytoplankton population are the aggregate of the proportional optical contributions from the cells and pigmentation suites of the representative species. For any one particular phytoplankton taxon, the optical properties may vary as a function of nutritional status, physiological state, and acclimation to environmental conditions (e.g., Geider, 1987; Schofield et al., 1995).

The optical-mass transform calculations are thus a fundamentally weak link in this chain. Mass is conserved, and IOPs are strictly additive; however, the relationship between mass and optical properties is not stationary in time and space. Furthermore, because it is the optical properties that impact the radiance signal that is ultimately detected by the satellite-based radiometer, attempts to provide satellite-based initial states and boundary values for a mass conservation modeling framework are likewise handicapped by the inherent uncertainty within the optical transforms. This inability to directly constrain mass partitions with satellite-based radiometer data also handicaps efforts to improve the veracity of internal transformation submodels (Q in Equation 4).

The Bio-Optical Forecasting (BioCast) system approach is to divest the short-term forecast framework

(hourly forecasts out to the 24–48 hour time horizon) from these weak links in the causal chain of optical variability. This is accomplished via ingestion of satellite-based optical products directly into the mass conservation framework as pseudo-tracers. In this approach, we retain the power of mass conservation and the utility of the synoptic satellite radiometer observations. A satellite-derived surface optical property becomes a pseudo-tracer (C'x), and the time-dependent changes in pseudo-tracer distributions can be estimated by an optical conservation equation of the form presented in Equation 4. For example, C'x may be set equal to beam attenuation at a reference wavelength (C'x = c_t(531 nm)). This obviates the requirement for the optical partition (Equation 1), the truncation of complex material constituents into bulk representative material classes (Equations 2–3), and the associated series of optical-mass transform calculations.

BioCast presumes that ocean circulation is fundamental to all else: the short-term change in pseudo-tracer distribution from the initial state (obtained directly from satellite data) to the future state is heavily weighted toward physical transport and the interaction of the physical transport with boundary values (also obtained from satellite data). The hypothesis is that the weighting is sufficiently heavy to effectively reduce internal optical property transformations to the null case ($Q = 0$ in Equation 4). Hence, the forecasting system must ingest and employ the satellite data as well as some estimate of the three-dimensional circulation to describe the time-dependent material transport. Operational and data-assimilative ocean circulation models provide these three-dimensional velocity fields (Rowley et al., 2014, and Allard et al., 2014, both in this issue).

BIOCAST: OPERATIONAL METHODS

BioCast software is designed to ingest modeled velocity fields and interpolate them to the spatial resolution consistent with the satellite image. The transport calculation is performed on a three-dimensional grid using a scaled and bathymetry-following vertical coordinate system down to a maximum depth of 200 m. In the initial implementation of BioCast, the pseudo-tracer (e.g., beam attenuation) vertical distribution is assumed to be homogenous. More complex vertical distributions for the initial state are considered in conjunction with the assimilation of in situ glider-based observations (see section on Future Work).

The fundamental key to the BioCast optical transport calculation is the integration of optical flux elements (OFEs).

These OFEs are the product of the optical pseudo-tracer (m^{-1}), the velocity (m s^{-1}), the BioCast internal time step (s), and the area dimensions of each face of the cubic BioCast grid cell (m^2) within the three-dimensional model grid. The optical pseudo-tracer is given a temporary unit reassignment from the native units (typically, m^{-1}) to mass per cubic meter, resulting in a pseudo-mass flux

for each OFE. This numerical method of transport computation is analogous to Eulerian first-order upstream differencing (Molenkamp, 1967). The BioCast internal time step is adjusted to consider the horizontal dimensions of the satellite image and numerical stability constraints. Forecast products are written to digital files on an hourly increment.

The Tactical Ocean Data System (TODS) is an operational software package that incorporates AOPS and other software components into a single user interface. The BioCast integration into TODS allows the user to link an AOPS satellite-processing region with operational ocean circulation model output in order to initiate a BioCast forecasting sequence. The sequence must begin with a complete satellite product field and a designation of land and ocean boundaries. An initially incomplete field is filled

> **BIOCAST SOFTWARE IS DESIGNED TO INGEST MODELED VELOCITY FIELDS AND INTERPOLATE THEM TO THE SPATIAL RESOLUTION CONSISTENT WITH THE SATELLITE IMAGE.**

in with interpolative techniques. Hourly ocean current forecasts are mapped to the three-dimensional BioCast grid and provide the basis for the transport calculation. Hourly BioCast optical property forecasts are then made available to the user. At the 24-hour forecast mark, the system looks for additional satellite data from AOPS to assimilate into the forecast sequence (Figure 4). The merger

missing data **AOPS**
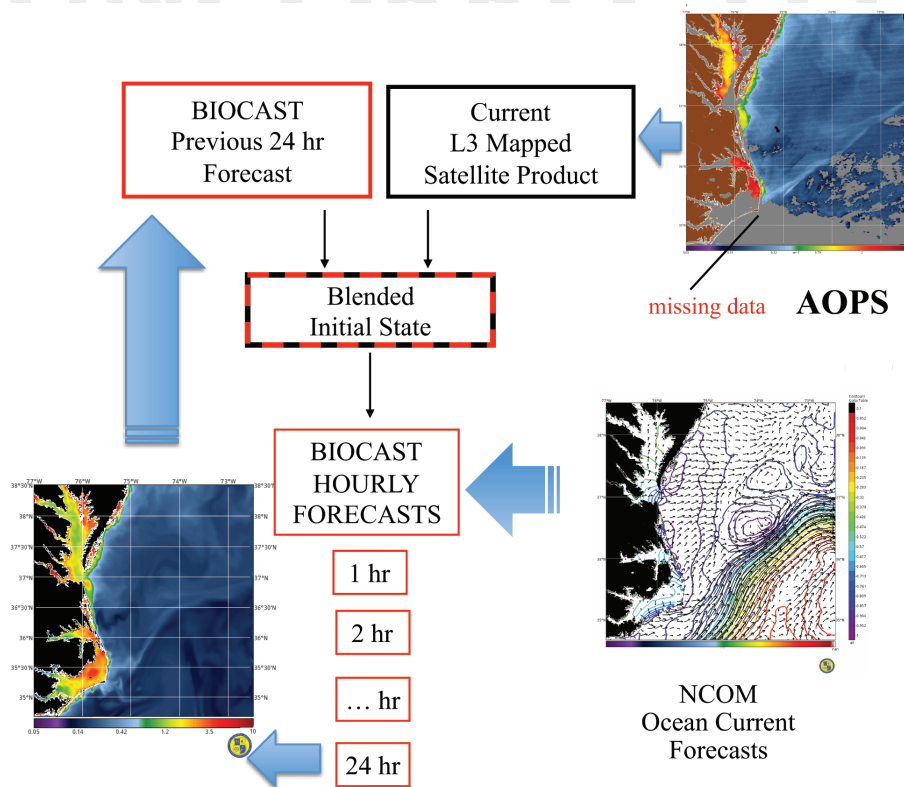

NCOM
Ocean Current
Forecasts

Figure 4. Diagram of the Bio-Optical Forecasting (BioCast) forecasting cycle: Navy Coastal Ocean Model (NCOM) velocity fields and daily mapped images are input to the system. The previous 24-hour forecast and the new image are merged to provide the initial state for a new forecast cycle.
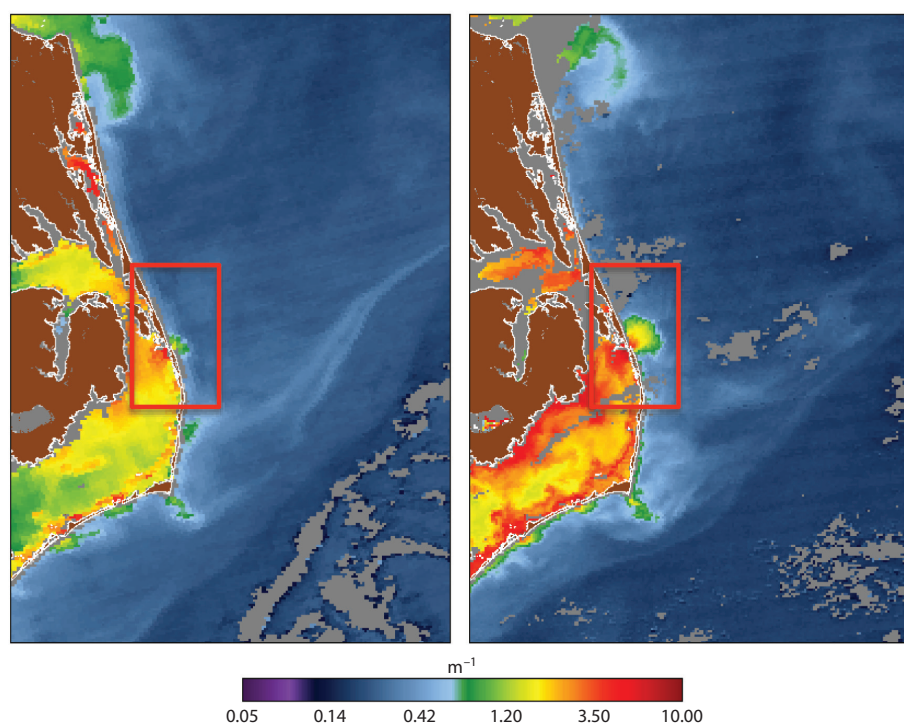

Figure 5. Moderate Resolution Imaging Spectroradiometer (MODIS) 1 km resolution image of beam attenuation for July 18, 2013 (left), and July 19, 2013 (right). Red inset is the expansion of a turbidity plume out of Orgeon Inlet, North Carolina.

■ CLDICE
■ LAND
■ ATMFAIL

of the 24-hour forecast and the new AOPS data stream constitutes a new initial state that initiates a new iteration of the forecast cycle. Once initiated, the BioCast system may iterate this forecast/update cycle autonomously.

BIOCAST RESULTS

Inner estuaries, sounds, and harbors are often turbid; the open ocean is comparatively clear. Coastal regions where sharp gradients between these extremes often occur are ideal test areas for an optical forecasting system. The US Naval exercise Trident Warrior-2013, conducted along the mid-Atlantic US East Coast, provided an opportunity to employ the BioCast system in real time. MODIS 1 km horizontal resolution optical products were ingested by the BioCast system along with regional Navy Coastal Ocean Model (NCOM; Barron et al., 2006) ocean current forecasts. BioCast produced 24-hour surface optical property forecasts that were subsequently merged with the next-day satellite image products to continuously iterate the forecast cycle (as in Figure 4) during July and August 2013.

Sequential MODIS imagery from July 18–19, 2013, reveals the seaward expansion of a turbidity plume from Oregon Inlet, North Carolina (Figure 5), a significant conduit of surface water flow between Pamlico Sound and the Atlantic Ocean. BioCast successfully forecasted this observed expansion (Figure 6a). From the initial state, the hourly forecasts progressively expand the 0.4 m^{-1} beam-c (531 nm) contour interval outward from Oregon Inlet an additional ~ 10–15 km northwest into the coastal ocean. Observed winds at the initialization time (1800 UTC July 18) are out of the southeast. Over the ensuing 24 hours, wind velocity triples and

wind direction shifts to the southwest. The simulation successfully predicts the surface current response to the changing winds: surface currents accelerate to a seaward trajectory and thereby transport turbid water away from Oregon Inlet, as was subsequently detected by satellite (Figures 5 and 6a).

Farther north, BioCast simulates the 24-hour seaward expansion of turbidity at the mouth of Chesapeake Bay and along the outer Virginia coastline (Figure 6b). The forecast expansion is accurate due to the underlying forecast models. The nested Coupled Ocean Atmosphere Prediction System (COAMPS®; Doyle et al., 2014, and Allard et al., 2014, both in this issue) accurately forecasts the displacement of an atmospheric high-pressure system settled in over the Appalachian Mountains by a continental low over the 24-hour forecast period. As a result, simulated southerly winds accelerate along the Virginia coastline. These

forecast coastal wind velocities are input to the NCOM, resulting in surface ocean current velocities oriented in an offshore direction. This information is used by BioCast to forecast an expansion of coastal turbidity that was subsequently confirmed by satellite.

STATISTICAL ANALYSIS

Episodes of observed expansion and contraction of surface optical isopleths against the US mid-Atlantic coastline were well captured by the BioCast system during the Trident Warrior exercise. Rather than describe all such cases with narrative detail, summary statistical measures are employed via comparison of the 24-hour forecast product with corresponding satellite data. In addition, persistence of present conditions is used as a benchmark metric for the veracity of the forecasting system. Failing any available forecasting system, the next best predictor of conditions tomorrow is likely to be the conditions today. The

inherent value of the forecasting system itself is thus evaluated with respect to the performance of persistence as a surrogate forecasting tool.

A single daily satellite product may contain significant areas of missing data due to clouds or atmospheric correction failure. Accordingly, the persistence values used were the 30-day latest image pixel composites rendered from the daily images over the previous 30 days. In other words, the value retained in each pixel is the last available datum for that space with a maximum latency of 30 days. The BioCast product (BC) and the 30-day latest-pixel composite persistence product (PS) were compared to the next-day satellite product.

Statistics from the 61-day forecast cycling period were first described in terms of the Mean Absolute Difference (MAD),

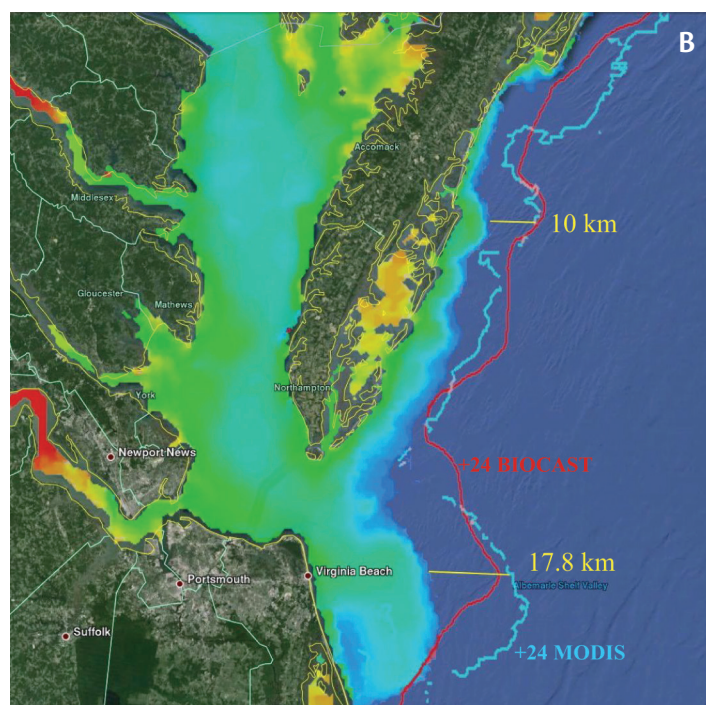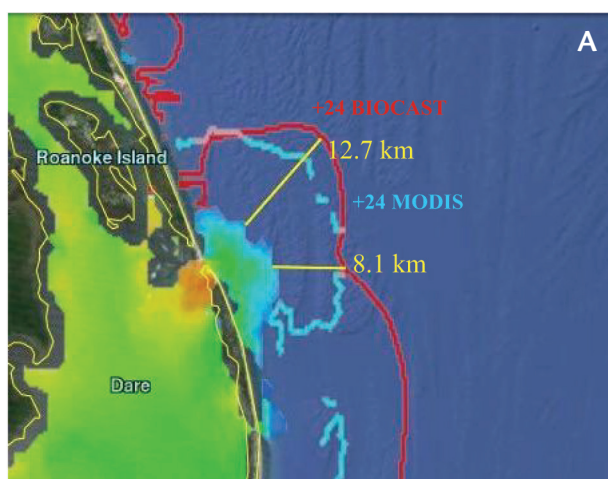$$MAD = \frac{1}{N} \sum_{n=1}^{N} |(F_n - R_n)| \qquad (5)$$

Figure 6. (A) Oregon Inlet, North Carolina: Beam attenuation contours for the initial state (July 18) and +24 hr (July 19). The initial contours terminate at c(531) = 0.4 m^{-1}. The 24 hour marks (red = BioCast, blue = MODIS) correspond to the c(531) = 0.4 m^{-1} optical isopleth. The yellow distance markers indicate the seaward expansion. The ocean color information is overlaid onto a Google Earth image projection. (B) As in (A), but for the Chesapeake Bay and Virginia coastline.

where *F* is the forecast product and *R* is the reference product (the next-day image pixel).

BioCast reduces the MAD for $c_t(531)$ by an average of ~ 51% over the various pixel inclusive distances from the coastline selected (10–249 km; Table 1). Beam-c values were also converted to horizontal diver visibility estimates to place the MAD statistics in more pragmatic terms. Again, the mean forecast field's departure from satellite data is reduced by approximately half when BioCast is used in place of persistence (Table 1).

Another method of analysis is to compare forecast model results using statistical summary diagrams. These diagrams depend upon reproducible relationships between statistical quantities to summarize different aspects of forecast model performance. These relationships assume the underlying probability density function of the variables is normal. Since the density function of ocean surface optical properties is log-normal (see Campbell, 1995), these raw data were log-transformed and converted to a "gray scale" following $GS[n] = \log_{10}(n) + 5.0$.

Performance statistics for BC and PS versus next-day imagery (*R*-reference) are first displayed on a normalized target diagram. The meaning of the target diagram is intuitively simple to understand:

the distance of a point from the origin is equal to the Root-Mean-Square (RMS) difference between the forecast product and the reference vector,

$$RMS = \left(\frac{1}{N} \sum_{n=1}^{N} (F_n - R_n)^2 \right)^{0.5} \qquad (6)$$

where RMS is normalized by the reference standard deviation ($RMS^* = RMS/\sigma_R$). The closer the point lies to the origin (bull's-eye), the better the RMS^* statistic (ideally, 0). The abscissa magnitude is the unbiased RMS^* (or pattern RMS^*) and the ordinate axis is the normalized bias (i.e., the difference between the mean of the comparison vectors). Further details may be found in Jolliff et al. (2009). For beam-c, PS values all fall in the RMS^* range $0.5 < PS < 1.0$ (Figure 7a). This is within acceptable limits of forecast performance. Situations where RMS^* values are greater than one suggest that a simple mean of the data would serve as a statistically superior forecast.

In contrast, BioCast (BC) target diagram performance measures (with the exception of the 10 km range) fall in the RMS^* range of $u^* < BC < 0.5$ (Figure 7a). These comparative performance measures lead to two conclusions: (1) BioCast provides a superior forecast product over persistence, and (2) there remains space for potential forecast

improvements. The latter conclusion is based on our estimate of the RMS^* uncertainty (u^*). In theory, there must be some point where improved forecast-data agreement is no longer meaningful due to inherent uncertainties in the observations. $RMS^* = u^*$ is the estimate of this uncertainty horizon.

Taylor diagrams provide another summary diagram format (Taylor, 2001). They are polar plots that examine the relationships between the linear correlation coefficient (radial axis) and the Standard Deviation Ratio ($SDR = \sigma_F/\sigma_R$). BioCast pattern measures (correlation and root variance) are all uniformly superior to persistence pattern measures over all ranges from the coastline considered (Figure 7b). This means the spatial distribution of surface optical properties in the BioCast forecast product is closer to the patterns revealed in the next-day satellite images than to those in persistence. This statistical result supports our hypothesis that satellite detected short-term (24 hr) variation in surface optical property distribution is driven primarily by ocean circulation.

The summary diagram statistical analyses were repeated for another AOPS product, the standard OC3 surface chlorophyll-*a* estimate (mg m^{-3}; O'Reilly et al., 2000). Satellite-estimated surface chlorophyll-*a* concentration is not a

Table 1. Beam-c/Horizontal Diver Visibility Mean Absolute Difference (MAD) Performance Statistics

Range	10 km	30 km	60 km	109 km	209 km	249 km
C (531 nm) MAD Persist. (m^{-1}) x 10^{-2}	29.80	17.17	10.95	8.37	6.57	5.93
C (531 nm) MAD BIOCAST (m^{-1}) x 10^{-2}	17.80	8.00	4.88	3.78	3.08	2.76
BioCast-C (531 nm) Difference Reduction (%)	40.3	53.4	55.4	54.8	53.1	53.5
Horizontal Diver Visibility MAD Persistence (m)	2.30	3.98	4.13	4.32	4.29	4.26
Horizontal Diver Visibility MAD BioCast (m)	1.50	1.63	1.73	1.73	2.04	1.97
BioCast-Diver Visibility Difference Reduction (%)	34.8	59.0	58.1	60.0	52.4	53.8
N (number of comparisons) =	2,532	11,046	23,039	35,757	54,110	65,337

surface optical property. On the other hand, this empirically based satellite product is probably not representative of genuine surface chlorophyll-*a* concentrations in many coastal regions due to the aforementioned optical complexities of these waters (e.g., Giannini et al., 2013). Satellite chlorophyll (or Csat) is more properly considered an index of water column light attenuation in many coastal situations. The summary diagram performance measures for Csat conform to the patterns for beam-c (Figure 7c,d): BioCast generally improves RMS* and pattern score statistical measures over persistence. We also note that at close

range (10–30 km), persistence falls just outside of RMS* = 1 and is thus an unacceptable forecast tool.

FUTURE DIRECTIONS

Operational forecasting is a performance-based endeavor. Highly complex and intricate ecosystem/material-transformation submodels are little more than superfluous baggage if they do not improve forecast performance. Similarly, boundary value schemes, numerical transport methods, and data assimilation techniques may all be modified in future versions of the software. However, these types of

modifications must demonstrate superior statistical forecast performance over BioCast (Version 1.0) before transition may be warranted. BioCast performance metrics for the 24-hour forecast sequence have been established for the Trident Warrior-2013 US Navy exercise and 10 months of continuous daily forecasting sequence trials in the northern Gulf of Mexico (data not shown).

Additional advancements in ocean optical forecasting will also result from the integration of BioCast with other TODS software components. For example, BioCast will be linked to system performance field estimation techniques
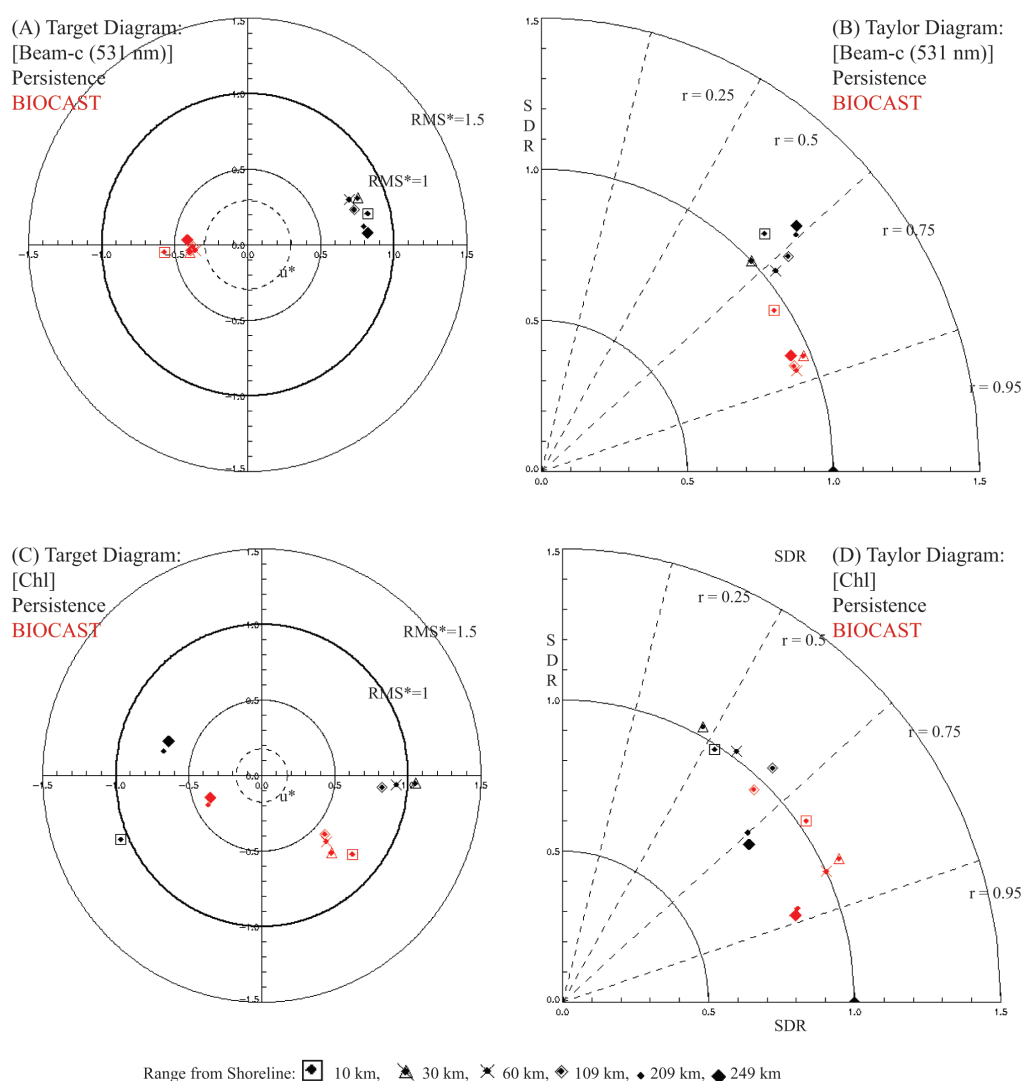

Figure 7. Statistical summary diagrams comparing 30-day latest pixel composites (persistence) against the next-day MODIS satellite product (black) and BioCast 24-hour forecast against the same next-day MODIS product (red). Statistics are generated from 61 days of "next-day" comparisons (July 2– August 31, 2013). The range refers to the subset of image pixels selected for statistical analysis using a distance from the shoreline criterion. Correlation (r) improves as the distance from the shoreline increases because the forecast products all mimic the general offshore bio-optical gradient.

Range from Shoreline: ⊡ 10 km, ▲ 30 km, ✖ 60 km, ◈ 109 km, ◆ 209 km, ◆ 249 km

for mine countermeasures operations. Vertical variations in optical properties can be estimated via the Three-Dimensional Optical Generator software package. This TODS component utilizes in situ data sent from autonomous underwater vehicles to derive statistical relationships between vertical optical variability and density variations in the

optimal tow height for the AN/AQS-24 above the ocean bottom, which is dependent on how efficiently the laser can penetrate the water column in order to discern potential bottom targets. A forecast of improved water column optical clarity can increase optimal tow heights for target identification and significantly reduce deployment time and asset

> " OPERATIONAL FORECASTING IS A PERFORMANCE-BASED ENDEAVOR. HIGHLY COMPLEX AND INTRICATE ECOSYSTEM/MATERIAL-TRANSFORMATION SUBMODELS ARE LITTLE MORE THAN SUPERFLUOUS BAGGAGE IF THEY DO NOT IMPROVE FORECAST PERFORMANCE. "

water column. These empirical optical property-density relationships are then projected to a three-dimensional field using (a) the AOPS satellite-radiometer products for the surface optical property values, and (b) density analysis fields from data-assimilative ocean models.

The final step in this performance field estimation technique is to serially link the vertical optical profiles with computer models that can estimate the performance of US Navy mine hunting systems under a variety of optical conditions. Forecast variations in the system performance may then provide a basis for optimal system deployment. For example, the AN/AQS-24 laser line scanner is a helicopter-towed underwater mine imaging system that is deployed by the US Navy's Helicopter Mine Countermeasures Squadrons (HM-14 "Vanguard" and HM-15 "Blackhawks"). The helicopter crew needs to know the

vulnerability. This is precisely the type of information that can enter into the tactical planning of naval missions, and it thereby completes the chain of research from first principles and basic science to accurate forecast products that support the US Navy and Marine Corps team.

ACKNOWLEDGMENTS

REFERENCES
Allard, R., E. Rogers, P. Martin, T. Jensen, P. Chu, T. Campbell, J. Dykes, T. Smith, J. Choi, and U. Gravois. 2014. The US Navy coupled air-ocean-wave prediction system. *Oceanography* 27(3):XX–XX, http://dx.doi.org/XXXX.

Barron, C.N., A.B. Kara, P.J. Martin, R.C. Rhodes, and L.F. Smedstad. 2006. Formulation, implementation and examination of vertical coordinate choices in the Global Navy Coastal Ocean Model (NCOM). *Ocean Modelling* 11:347–375, http://dx.doi.org/10.1016/j.ocemod.2005.01.004.

Binding, C.E., D.G. Bowers, and E.G. Mitchelson-Jacob. 2005. Estimating suspended sediment concentrations from ocean colour measurements in moderately turbid waters: The impact of variable particle scattering properties. *Remote Sensing of Environment* 94:373–383, http://dx.doi.org/10.1016/j.rse.2004.11.002.

Caesar, G.J. 56 BCE. *Comentarii de Bello Gallico*. The Gallic Wars, Book 3. As translated by W.A. McDevitte and W.S. Bohn, 1869. New York, Harper & Brothers.

Caesar, G.J. 55 BCE. *Comentarii de Bello Gallico*. The Gallic Wars, Book 4. As translated by W.A. McDevitte and W.S. Bohn, 1869. New York, Harper & Brothers.

Campbell, J.W. 1995. The lognormal distribution as a model for bio-optical variability in the sea. *Journal of Geophysical Research* 100(C7):13,237–13,254, http://dx.doi.org/10.1029/95JC00458.

Chang, G., K. Mahoney, A. Briggs-Whitmire, D.D.R. Kohler, C.D. Mobley, M. Lewis, M.A. Moline, E. Boss, M. Kim, W. Philpot, and T.D. Dickey. 2004. The new age of hyperspectral oceanography. *Oceanography* 17(2):16–23, http://dx.doi.org/10.5670/oceanog.2004.43.

Corson, M.R., and C.O. Davis. 2011. A new view of the coastal oceans from the space station. *Eos Transactions, American Geophysical Union* 92(19):161, http://dx.doi.org/10.1029/2011EO190001.

Cunningham, A., D. McKee, S. Craig, G. Tarran, and C. Widdicombe. 2003. Fine-scale variability in phytoplankton community structure and inherent optical properties measured from an autonomous underwater vehicle. *Journal of Marine Systems* 43:51–59, http://dx.doi.org/10.1016/S0924-7963(03)00088-5.

Doyle, J., R.M. Hodur, S. Chen, Y. Jin, J.R. Moskaitis, S. Wang, E.A. Hendricks, H. Jin, and T.A. Smith. 2014. Tropical cyclone prediction using COAMPS-TC. *Oceanography* 27(3):XX–XX, http://dx.doi.org/XXXX.

Geider, R.J. 1987. Light and temperature dependence of the carbon to chlorophyll ratio in microalgae and cyanobacteria: Implications for physiology and growth of phytoplankton. *New Phytologist* 106:1–34, http://dx.doi.org/10.1111/j.1469-8137.1987.tb04788.x.

Giannini, M.F.C., C.A.E. Garcia, V.M. Tavano, and Á.M. Ciotti. 2013. Effects of low-salinity and high-turbidity waters on empirical ocean colour algorithms: An example for Southwestern Atlantic waters. *Continental Shelf Research* 59:84–96, http://dx.doi.org/10.1016/j.csr.2013.04.013.

Jolliff, J.K., J.C. Kindle, I. Shulman, B. Penta, M.A.M. Friedrichs, R. Helber, and R.A. Arnone. 2009. Summary diagrams for coupled hydrodynamic-ecosystem model skill assessment. *Journal of Marine Systems* 76:64–82, http://dx.doi.org/10.1016/j.jmarsys.2008.05.014.

Kowalczuk, P., W.J. Cooper, M.J. Durako, A.E. Kahn, M. Gonsior, and H. Young. 2010. Characterization of dissolved organic matter fluorescence in the South Atlantic Bight with use of PARAFAC model: Relationships between fluorescence and its components, absorption coefficients and organic carbon concentrations. *Marine Chemistry* 118:22–36, http://dx.doi.org/10.1016/j.marchem.2009.10.002.

Ladner, S., A. Lawson, P. Martinolich, J. Bowers, G. Fargion, and R. Arnone. 2013. *Validation Test Report for the Automated Optical Processing System (AOPS) Version 4.8*. US NRL Technical Memorandum Report. NRL/MR/7330—13-9465, http://oai.dtic.mil/oai/oai?verb=getRecord&metadataPrefix=html&identifier=ADA588071.

Lewis, D., R.W. Gould, A. Weidemann, S. Ladner, and Z. Lee. 2013. Bathymetry estimations using vicariously calibrated HICO data. In *Proceedings of SPIE* 8724. Ocean Sensing and Monitoring V, 87240N, http://dx.doi.org/10.1117/12.2017864.

Metzger, E.J., O.M. Smedstad, P.G. Thoppil, H.E. Hurlburt, J.A. Cummings, A.J. Wallcraft, L. Zamudio, D.S. Franklin, P.G. Posey, M.W. Phelps, and others. 2014. US Navy operational global ocean and Arctic ice prediction systems. *Oceanography* 27(3):XX–XX, http://dx.doi.org/XXXX.

Mobley, C.D. 1994. *Light and Water*. Academic Press, San Diego, CA, 595 pp.

Molenkamp, C.R. 1967. Accuracy of finite-difference methods applied to the advection equation. *Journal of Applied Meteorology* 7:160–167, http://dx.doi.org/10.1175/1520-0450(1968)007<0160:AOFDMA>2.0.CO;2.

O'Reilly, J.E., S. Maritorena, M.C. O'Brien, D.A. Siegel, D. Toole, D. Menzies, R.C. Smith, J.L. Mueller, B.G. Mitchell, M. Kahru, and others. 2000. *Postlaunch Calibration and Validation Analysis, Part 3*. NASA Technical Memorandum 2000-206892, vol., 11, SeaWIFS Postlaunch Technical Report Series, S.B. Hooker and E.R. Firestone, eds, NASA Goddard Space Flight Center, 49 pp., http://oceancolor.gsfc.nasa.gov/REPROCESSING/SeaWiFS/R3/Documents/postlaunch_Volume11.pdf.

Rhodes, R.C., H.E. Hurlburt, A.J. Wallcraft, C.N. Barron, P.J. Martin, O.M. Smedstad, S.L. Cross, and A.B. Kara. 2002. Navy real-time global modeling systems. *Oceanography* 15(1):29–43, http://dx.doi.org/10.5670/oceanog.2002.34.

Rowley and Mask. 2014. XXXXXX. *Oceanography* 27(3):XX–XX, http://dx.doi.org/XXXX.

Schofield, O., T. Bergmann, M.J. Oliver, A. Irwin, G. Kirkpatrick, W.P. Bissett, M.A. Moline, and C. Orrico. 2004. Inversion of spectral absorption in the optically complex coastal waters of the Mid-Atlantic Bight. *Journal of Geophysical Research* 109, C12504, http://dx.doi.org/10.1029/2003JC002071.

Schofield, O., M.M. Moline, and B.B. Prezelin. 1995. Palmer LTER: Photoacclimation in a coastal phytoplankton bloom. *Antarctic Journal of the United States* 30(5):260–262.

Siegel, D.A., S. Maritorena, N.B. Nelson, D.A. Hansell, and M. Lorenzi-Kayser. 2002. Global distribution and dynamics of colored dissolved and detrital organic materials. *Journal of Geophysical Research* 107(C12):3,228, http://dx.doi.org/10.1029/2001JC000965.

Sournia, A., M.-J. Chrdtiennot-Dinet, and M. Richard. 1991. Marine phytoplankton: How many species in the world ocean? *Journal of Plankton Research* 13:1,093–1,099, http://dx.doi.org/10.1093/plankt/13.5.1093.

Taylor, K.E. 2001. Summarizing multiple aspects of model performance in a single diagram. *Journal of Geophysical Research* 106(D7):7,183–7,192, http://dx.doi.org/10.1029/2000JD900719.

Vegetius Renatus, P.F. 432 (est.). *Epitoma rei militaris, sive institutorum rei militaris libri quinque*. As translated by P.D. Emanuele in "Vegetius on the Roman Navy: Translation and Commentary, Book Four, 31–46," MA Thesis, University of British Columbia, 1974.

Vodacek, A., N.V. Blough, M.D. DeGrandpre, E.T. Peltzer, and R.K. Nelson. 1997. Seasonal variation of CDOM and DOC in the Middle Atlantic Bight: Terrestrial inputs and photooxidation. *Limnology and Oceanography* 42(4):674–688, http://dx.doi.org/10.4319/lo.1997.42.4.0674.

Zaneveld, J.R.V., and W.S. Pegau. 2003. Robust underwater visibility parameter. *Optics Express* 11:2,997–3,009, http://dx.doi.org/10.1364/OE.11.002997.